

The Optical/Infrared Astronomical Quality of High Atacama Sites.

II. Infrared Characteristics

RICCARDO GIOVANELLI, JEREMY DARLING, CHARLES HENDERSON, WILLIAM HOFFMAN, DON BARRY, JAMES CORDES,
STEPHEN EIKENBERRY, GEORGE GULL, LUKE KELLER, J. D. SMITH, AND GORDON STACEY

Department of Astronomy, Cornell University, Ithaca, NY 14853; riccardo@astrosun.tn.cornell.edu

Received 2001 January 3; accepted 2001 March 11

ABSTRACT. We discuss properties of the atmospheric water vapor above the high Andean plateau region known as the Llano de Chajnantor, in the Atacama Desert of northern Chile. A combination of radiometric and radiosonde measurements indicates that the median column of precipitable water vapor (PWV) above the plateau at an elevation of 5000 m is approximately 1.2 mm. The exponential scale height of the water vapor density in the median Chajnantor atmosphere is 1.13 km; the median PWV is 0.5 mm above an elevation of 5750 m. Both of these values appear to be lower at night. Annual, diurnal, and other dependences of PWV and its scale height are discussed, as well as the occurrence of temperature inversion layers below the elevation of peaks surrounding the plateau. We estimate the background for infrared observations and sensitivities for broadband and high-resolution spectroscopy. The results suggest that exceptional atmospheric conditions are present in the region, yielding high infrared transparency and high sensitivity for future ground-based infrared telescopes.

1. INTRODUCTION

Atmospheric molecules are responsible for band absorption of cosmic radiation. In the near- and mid-IR, the most important absorbers are the triatomic molecules H₂O, CO₂, and O₃.

Between absorption bands, partially transparent windows appear, making astronomical observations possible in the near- and mid-IR from the ground. The atmosphere is virtually opaque between 50 and 200 μ m from all sites on the ground, making that wavelength region the exclusive territory of airborne and space observatories. Water vapor also dominates absorption in the far-IR and submillimeter regimes; atmospheric windows appear near 200, 350, 450, 600, 750, and 870 μ m; in these spectral regimes transparency is significant only in dry, high-altitude sites (Tokunaga 2000; Wolfe & Zissis 1978). H₂O molecules have a short residence time (a few days) in the atmosphere, and their concentration is highly variable. Thus, the characterization of potential astronomical sites for operation in the IR and submillimeter spectral regimes depends very strongly on measurements of atmospheric water vapor.

In a companion paper (Giovannelli et al. 2001, hereafter Paper I), we have discussed the desirability of ascertaining the quality of high-altitude sites for astronomical research in the optical and infrared parts of the spectrum. Paper I describes briefly the Atacama desert region and, as part of a site survey campaign, the results of optical seeing measurements. Here we review the results of measurements carried out in the Andean plateau known as the Llano de Chajnantor, in the Atacama Desert of northern Chile, aimed at gauging the atmospheric transparency and emissivity in the infrared. The main char-

acteristics of the atmospheric water vapor in the region are discussed: its absolute amount, annual, seasonal, and diurnal variations, as well as its vertical distribution. The latter information provides indications of the relative infrared transparency at sites at varying elevation above the plateau, even of those currently inaccessible for the deployment of testing equipment.

In § 2 we briefly describe the data utilized for the analysis; in § 3 statistics of the total precipitable water vapor (PWV, defined as the atmospheric column density of water vapor) are given, and in § 4 the vertical distribution of PWV is analyzed, with estimates of its value expected for candidate sites for an optical/IR telescope. Finally, in § 5 we estimate atmospheric transparency, emissivity, and telescope sensitivities in the infrared, for a range of possible water vapor conditions.

2. DATA SOURCES

We make use of two kinds of data in this report:

1. Atmospheric opacities measured with automated tipping radiometers at 225 GHz and at 183 GHz. These instruments are operated by the National Radio Astronomy Observatory (NRAO), the European Southern Observatory (ESO), and the Onsala Space Observatory. Data taken since 1995 April can be found on-line.¹ We shall refer to summaries of relevant data products as given at those sites.

¹ See the NRAO Chajnantor Site Data page, maintained by S. Radford (<http://www.tuc.nrao.edu/mma/sites/Chajnantor/data.c.html>), and the ALMA Site Characterization page (<http://alma.sc.eso.org>).

2. Radiosonde data from balloon launches initiated in 1998 October, jointly operated by Cornell University, NRAO, ESO, and the Smithsonian Astrophysical Observatory. We will summarize results from radiosondes launched between 1998 October and 2000 August. Details on individual launches can be found on-line² and at the NRAO and ESO Web sites.³ A more detailed analysis of the full radiosonde data set will be presented in a forthcoming paper, by the radiosonde consortium.

Tipping radiometers yield values of the atmospheric opacity, from which estimates of PWV above the radiometer location can be inferred. Radiosondes, on the other hand, provide vertical profiles of atmospheric parameters (temperature, pressure, relative humidity, wind speed, and direction); from those, the water vapor density distribution and thus the PWV above any altitude can be inferred. Several summits, which are potentially attractive sites for infrared telescopes, have no access roads, and thus installation and access to equipment at those locations is impractical. The free atmosphere parameters obtained from radiosonde launches provide a rough approximation of conditions that would be found at those summits. In the remainder of this paper, we shall always refer to PWV at zenith.

The sites for radiometer data taking and radiosonde launches are within 1 km from each other, near latitude S23°01', longitude W67°46', at an altitude near 5000 m above mean sea level. It should be kept in mind that, depending on wind speed and direction, a sonde flight samples an oblique path through the atmosphere, rather than a vertical one. In strong wind, a sonde profile typically spans tens of kilometers in horizontal range. However, since most of the atmospheric water vapor is generally distributed within a few kilometers from the ground, the effective sampling of most of the PWV corresponds to a horizontal range of only a few kilometers from the launch site. Given the prevalent wind direction (see Paper I for details), sondes usually fly toward the east over unpopulated terrain, with ground elevation ranging between 4500 and 5800 m above mean sea level.

In this paper, we shall use data from 108 radiosonde launches distributed as follows: 8, 10, and 16 launches in 1998 October, November, and December, respectively; 1, 5, and 33 in 1999 February, March, and November, respectively; 11, 18, and 6 in 2000 June, July, and August, respectively. Thirty were launched in nighttime hours (0100–1100 UT), 65 in daytime (1200–2100 UT), and 13 in the early evening (2200–0000 UT). For each sonde profile we integrate the water vapor to obtain PWV above the plateau level of 5050 m, above the elevation of 5400 m (equivalent to the summit of Cerro Honar), and

above 5750 m (equivalent to the summit of Cerro Chascón). We also compute the height above the plateau at which water vapor density drops to $1/e$ of the value at the plateau level, h_e , an indication of the exponential scale height of the water vapor layer. Since the water vapor distribution is most often not close to an exponential, we also measure $h_{1/2}$, the height at which PWV drops to 50% of the value at the plateau level. Finally, we note the location of temperature inversions, which often are seen trapping large fractions of the total PWV below them. The derivation of these parameters and a detailed presentation of the sonde data will be given in a consortium paper, as mentioned above.

3. PRECIPITABLE WATER VAPOR ABOVE 5000 m

The conversion from radio opacities to PWV can be obtained from models of the atmosphere and assumptions on the water vapor line shapes. These are usually fairly uncertain, especially in the case of 225 GHz observations (e.g., see Holdaway et al. 1996a, 1996b). The conversion is more reliable in the case of 183 GHz data, for the nearby water line is stronger and the “wet” contribution to the opacity larger. Delgado et al. (1999) give a reliable conversion relation directly from antenna temperature to PWV from 183 GHz observations and have also derived a conversion relation from τ_{225} to PWV, which we use:

$$\tau_{225} = 0.0435(\text{PWV}) + 0.0068. \quad (1)$$

On the basis of preliminary comparisons, equation (1) yields good agreement with PWV derived from radiosonde data for values of PWV < 3 mm; for higher values, however, PWV may be overestimated by equation (1). Fortunately, the latter cases are of relatively less interest in our case.

The most extensive database of radiometric opacities at the Chajnantor Plateau is that derived from the NRAO database.⁴ The historical quartiles between 1995 April and 2000 April are respectively 0.036, 0.060, and 0.114, which convert to PWV values of respectively 0.67, 1.22, and 2.46 mm. The PWV quartiles of 108 radiosonde flights between 1998 October and 2000 August are 0.71, 1.04, and 1.85 mm. The difference between radiosonde and tipping radiometry values of PWV is not very surprising, for variations in the median PWV from year to year are large and the time interval for sonde launches is less than 2 years. Moreover, the radiosonde launches under-emphasize the summer season, when PWV is much larger than in the rest of the year. The value of PWV inferred from radiometry provides a more reliable long-term estimate for the Chajnantor Plateau, although it should be kept in mind that the epoch of radiometry measurements includes the exceptional

² See the Large Atacama Telescope Radiosonde Flights page (http://www.astro.cornell.edu/atacama/site_survey/sondedata.html).

³ See the NRAO/ALMA page (<http://www.tuc.nrao.edu/mma/sites/Chajnantor/data.c.html>) and ESO/ALMA page (<http://alma.sc.eso.org/htmls/radiosonde.html>).

⁴ See the NRAO Chajnantor Site Data page, maintained by S. Radford (<http://www.tuc.nrao.edu/mma/sites/Chajnantor/data.c.html>).

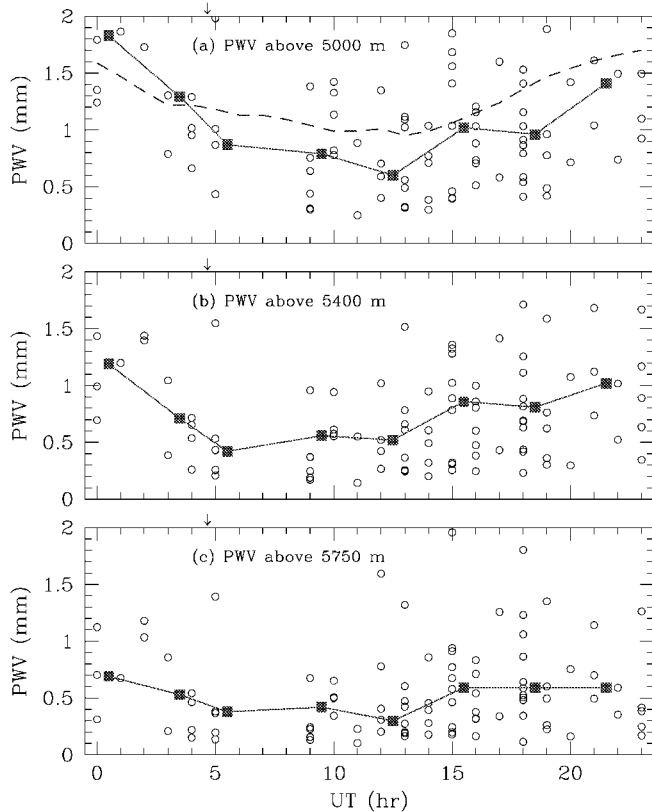


FIG. 1.—PWV as obtained from radiosonde profiles. The water vapor density is integrated above 5000, 5400, and 5750 m. *Open circles*, individual sonde profiles; *filled squares*, running medians over 3 hr intervals. Midnight is at 0431 UT, as indicated by the vertical arrow on top of each panel.

El Niño/La Niña episode of 1997–1998, the most extreme on record (McPhaden 1999), which may bias upward the PWV median.

Seasonal variations in PWV are conspicuous. In the months of January and February, PWV is several times higher than in the winter months. This is the result of moist Amazon air flowing from the northeast, a condition locally referred to as “Bolivian winter” and often accompanied by precipitation above 4000 m elevation. Inspection of the 225 GHz radiometry record indicates that the median PWV at Chajnantor between March and early December is less than 1 mm.

The diurnal cycle also affects PWV, which tends to be higher in the afternoon hours, followed by a rapid decrease after sunset. Figure 1 displays the diurnal variation of PWV above 5000, 5400, and 5750 m, top to bottom respectively, as derived from radiosonde data (*unfilled circles*). Median values over 3 hr intervals are indicated as large, filled squares, connected by a solid line. The dashed line displays the median values of PWV, as obtained from 225 GHz opacities at 5000 m. Local midnight takes place at 0431 UT. The atmosphere appears to be driest in the late part of the night and early part of the morning.

TABLE 1
PWV (IN mm) QUANTILES FOR 108 RADIOSONDES

Quartile	5000 m	5400 m	5750 m	<i>N</i>
All:				108
25%	0.71	0.40	0.27	
50%	1.04	0.72	0.49	
75%	1.75	1.28	0.92	
Day:				65
25%	0.58	0.40	0.32	
50%	1.04	0.82	0.54	
75%	1.75	1.33	1.00	
Night:				30
25%	0.76	0.37	0.21	
50%	1.00	0.57	0.42	
75%	1.42	1.05	0.68	
0500–1300 UT:				32
25%	0.46	0.26	0.20	
50%	0.85	0.53	0.36	
75%	1.23	0.86	0.63	

The diurnal cycle of PWV lags in phase the sunlight cycle by about 4 hours and has an amplitude of about 20% about the median value.

4. VERTICAL DISTRIBUTION OF PRECIPITABLE WATER VAPOR

Table 1 displays quartile values of PWV above 5000, 5400, and 5750 m for four different groupings of the radiosonde flights: in addition to the daytime and nighttime sets described in § 2, we also use the combined set of 108 sondes (“All”) and that of 32 sondes launched between 0500 and 1300 UT. The latter corresponds to the UT interval in which the minimum of the diurnal cycle is seen. We note that with respect to the value of PWV at the plateau level overall, PWV drops by 30% in the first 400 m and by a factor of 2 in the first 750 m above the plateau. That decrease may be even steeper during nighttime hours, suggesting that the effective thickness of the water vapor layer decreases at night. While the absolute values of PWV listed in Table 1 may be lower than historical values, as indicated by the comparison with 225 GHz opacities and discussed in the preceding section, the variation of PWV with elevation is reliable.

Whether the decrease in PWV with height will be that of the free atmosphere indicated in Table 1, or lower, will depend on the local topography, the area of the summits, the direction of the wind, and other factors. However, it is clear that by accessing higher ground above the plateau, significant gains in terms of infrared transparency and background emission can be obtained.

The thickness of the water vapor layer can be measured by h_e or $h_{1/2}$. For the set of 108 radiosondes, we find the following quartile values: $h_{1/2}(25\%) = 571$ m, $h_{1/2}(50\%) = 836$ m, $h_{1/2}(75\%) = 1083$ m; and $h_e(25\%) = 836$ m, $h_e(50\%) = 1135$ m, $h_e(75\%) = 1504$ m. Examining the relative humidity

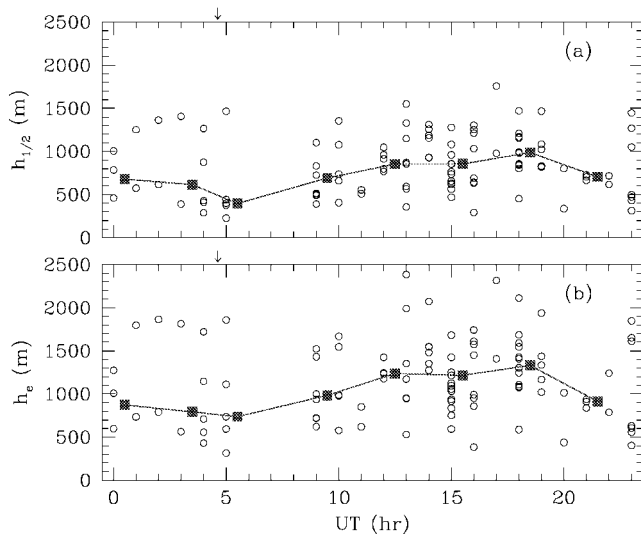


FIG. 2.—Half-thickness and scale height of the water vapor layer, as obtained from radiosonde profiles. *Open circles*, individual sonde profiles; *filled squares*, running medians over 3 hr intervals. Midnight is at 0431 UT, as indicated by the vertical arrow on top of each panel.

records from stations at different elevations at the Japanese testing site of Rio Frio, a region to the south of the Chajnantor Plateau, Holdaway et al. (1996a, 1996b) found indications that the scale height of the water vapor layer may vary with the diurnal cycle, between values of approximately 2 and 1 km, the low value being attained at night. Figure 2 yields support for that suggestion. Values of h_e and $h_{1/2}$ for each in the set of 108 radiosonde flights are displayed against time of day. Median values are identified by large filled squares. A diurnal oscillation in the thickness of the water layer, of amplitude near 25% about its median value, may be present. The cycle appears to be in phase with that of the solar illumination cycle. The statistical significance of this result is low, the lack of sonde launches between 0400 and 0900 UT being particularly important in this respect. We next present corroborating evidence regarding this potentially important result.

In Figure 3 we show the vertical distribution of the water vapor density in the Chajnantor median atmosphere (similar plots for the temperature distribution and the wind speed are shown in Paper I). The thick solid line tracks the median water vapor density profile over the plateau between April and December, from 108 radiosonde profiles. The distribution is well approximated by an exponential with scale height $h_e = 1.135$ km, as discussed above. The median profiles for day and night radiosonde launches do however depart significantly from exponential behavior: during night, more water vapor is found at lower elevations; i.e., the effective thickness of the water layer decreases. As pointed out in the previous section, median PWV between 0100 and 1100 UT (night) is about the same as between 1200 and 2100 UT (day), although

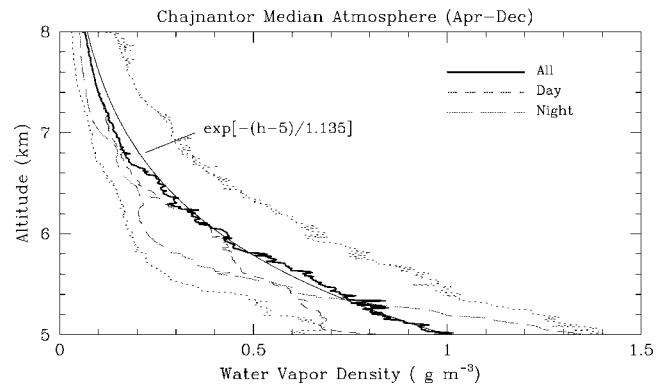


FIG. 3.—Distribution of the water vapor density in the median atmosphere over the Chajnantor Plateau. *Thick solid line*, the median water vapor density, at each altitude, from 108 radiosonde profiles; *dotted lines*, 25% and 75% quartiles about that median; *thin solid line*, exponential of scale height 1.135 km. *Short-dashed line*, median profile for 65 daytime sondes; *long-dashed line*, median profile for 30 nighttime sondes.

the median value between 0500 and 1300 UT is significantly lower.

On any given time, the departures of the water vapor distribution from an exponential can be quite severe. Figures 4, 5, and 6 display data for three different radiosonde launches. In panel *a* of each figure, the air temperature and the dew point temperature are displayed; in panel *b*, wind speed and direction are shown; in panel *c*, the relative humidity and the water vapor pressure are given, while in panel *d* we have the water vapor density and PWV. The temperature and water vapor profiles of Figure 4 are unusually smooth. The water vapor density distribution appears exponential, with a scale height of about 1420 m. Profiles such as that tend to be the exception. More often, temperature inversions are present, and the water vapor distribution is raggedly uneven. In the case of Figure 5, for example, two prominent temperature inversions take place near altitudes of 6600 and 8200 m. The atmospheric water vapor lies mostly under the lower of the two inversion layers, and the vertical distribution of the water vapor density is far from exponential in shape. In Figure 6, an inversion layer is present near 5300 m, and half of all water vapor above the Chajnantor Plateau is packed in the lowest 400 m of atmosphere. Were circumstances such as that displayed in Figure 6 frequent, peaks that rise several hundred meters above the plateau would be highly attractive candidate sites for infrared observations. We have reviewed all radiosonde profiles and selected those for which temperature inversion layers can be identified. In Figure 7, we plot the altitude of the lowest (in the case in which more than one is discernible) inversion visible in the temperature profile, separately for day and night radiosonde flights. The fraction of temperature inversions taking place below 500 m above the plateau level is far larger during the night than during the day, by an amply significant margin. The

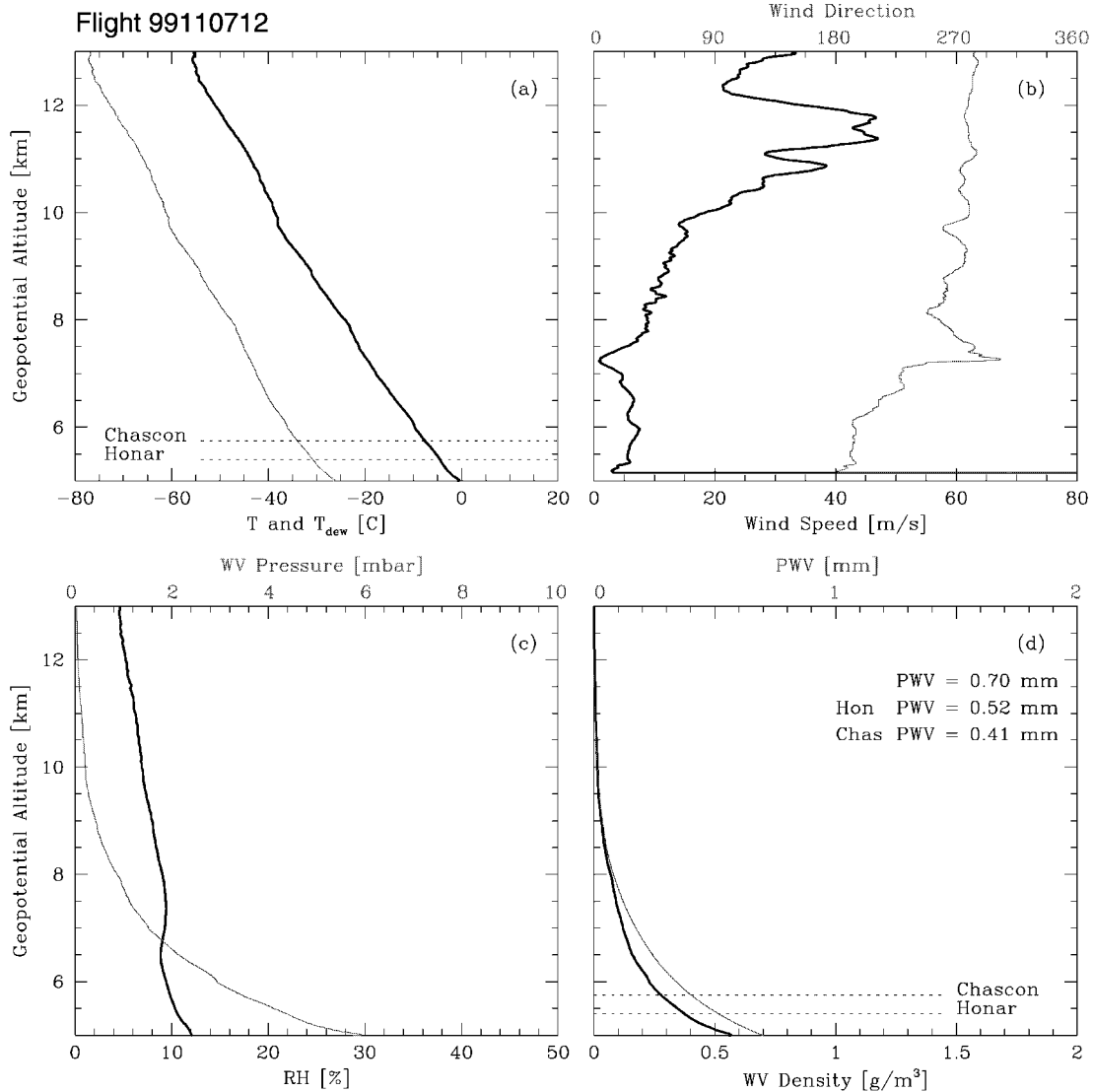


FIG. 4.—Radiosonde atmospheric profiles. *Upper left*: temperature (*thick line*) and dew point temperature (*thin line*). *Upper right*: wind speed (*thick*) and direction (*thin line*). *Lower left*: relative humidity (*thick line*) and water vapor pressure (*thin line*). *Lower right*: water vapor density (*thick line*) and PWV (*thin line*). The horizontal dotted lines are at the elevations of Cerro Honar (5400 m) and Cerro Chascón (5750 m). Unusually smooth atmospheric conditions are sampled by this sonde flight of 1999 November 7, 1200 UT. No strong temperature inversions are seen in the lower atmosphere.

nightly decrease in the thickness of the water vapor layer appears to be related to the development of temperature inversions close to the ground.

The occurrence and altitude of temperature inversions is of importance not only for their impact on the PWV, and thus the infrared transparency, of a site, but also for the quality of astronomical seeing. Evidence exists (Hufnagel 1978) that in those layers large values of the refractive index structure constant C_n^2 occur. The seeing disk of stellar images, $\theta_{\text{hpfrw}} \propto \int C_n^2 dz$, can thus be strongly affected. A site above the inversion layer would hence yield better astronomical image quality.

5. ATMOSPHERIC TRANSPARENCY IN THE INFRARED

5.1. Atmospheric Transparency and Thermal Background

Figure 8 displays curves of atmospheric transparency at zenith, computed for a site at an altitude of 5000 m and different column densities of water vapor above head, for the window between $5 \mu\text{m}$ and 1mm . In the spectral region between 50 and $200 \mu\text{m}$ the atmosphere is quite opaque from all ground sites: even if PWV were as low as $100 \mu\text{m}$, transparency would not reach 40%. However, the window near $200 \mu\text{m}$ may be of

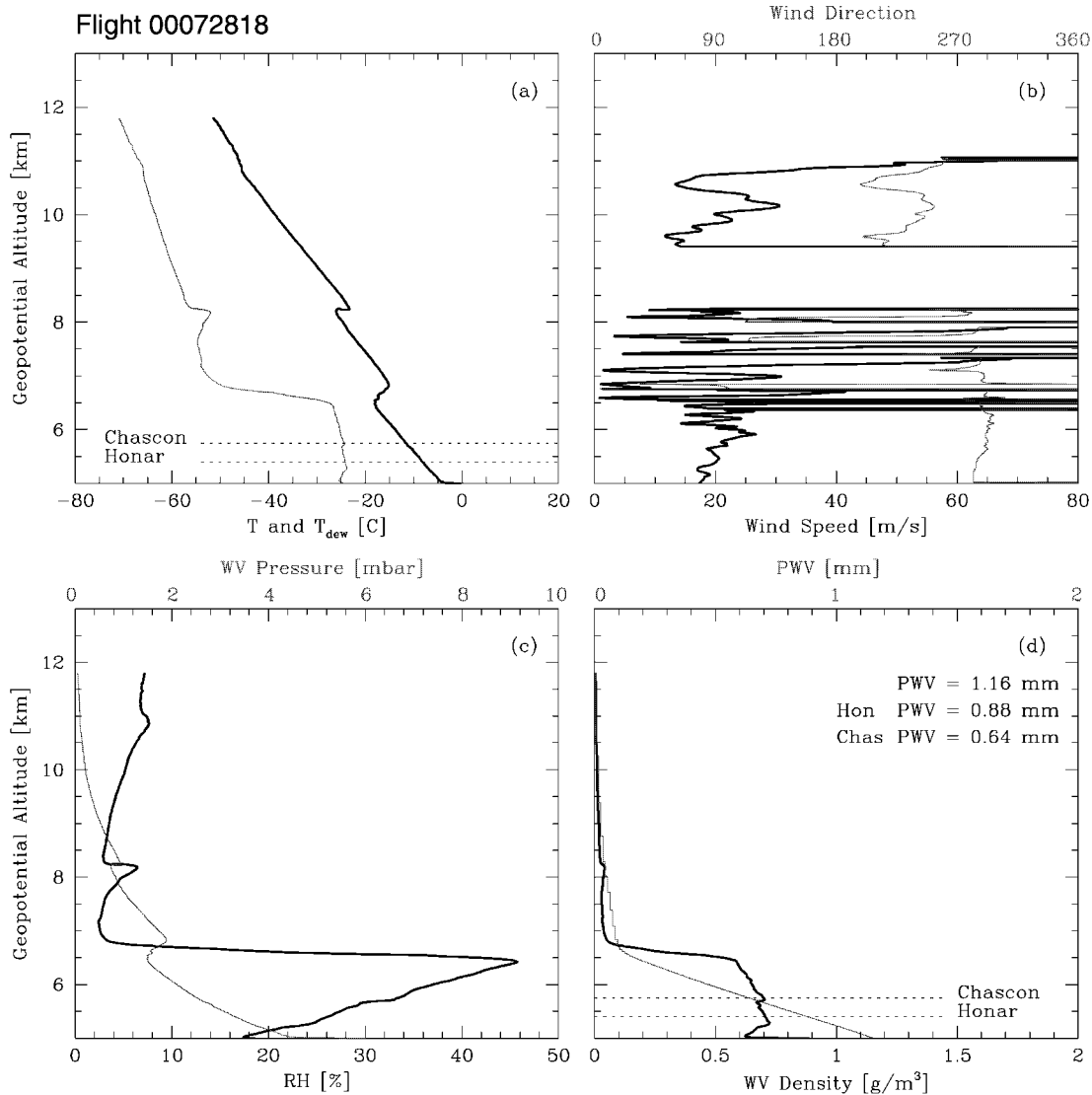


FIG. 5.—Radiosonde data for a 2000 July 28 launch, 1800 UT. Temperature inversions appear near 6.6 and 8.2 km. Notice also the large increase in humidity below the 6.6 km inversion layer. The raggedness of the wind data is due to poor sonde tracking. Panel description as in Fig. 4.

interest for observations of the very important spectral line of C^+ . For low values of PWV, numerous atmospheric windows appear longward of $10 \mu\text{m}$, notably near 20, 24, 32, 34, 38, 42, and $46 \mu\text{m}$.

The main deleterious effects of the atmosphere on astronomy consist of reduced transparency to cosmic photons from a given line of sight, seeing degradation of optical and infrared images, and an increase of the diffuse background, against which the generally weak signals of cosmic sources need to be discriminated. The effective temperature of the most relevant atmospheric layers is between 200 and 300 K, so the atmospheric thermal emission peaks near $15 \mu\text{m}$. Near the centers of the absorption bands where the atmosphere is opaque, a maximum

background flux is reached and, of course, no cosmic photons get through. In spectral regions of partial transparency, the atmospheric background radiation can be approximated by that of a blackbody attenuated by a factor which is the complement of the transparency. If opacity is distributed over a wide range of elevations, this assumption may be flawed; it is however a good approximation for the opacity produced by water vapor, which is found very close to the ground, and is our main concern in this paper. In the optical and near-IR, the principal source of atmospheric background during the day is the scattering of solar radiation. At night, however, airglow in the near-IR results from transitions between vibrational states of the OH^- radical, discharging energy stored during daytime from

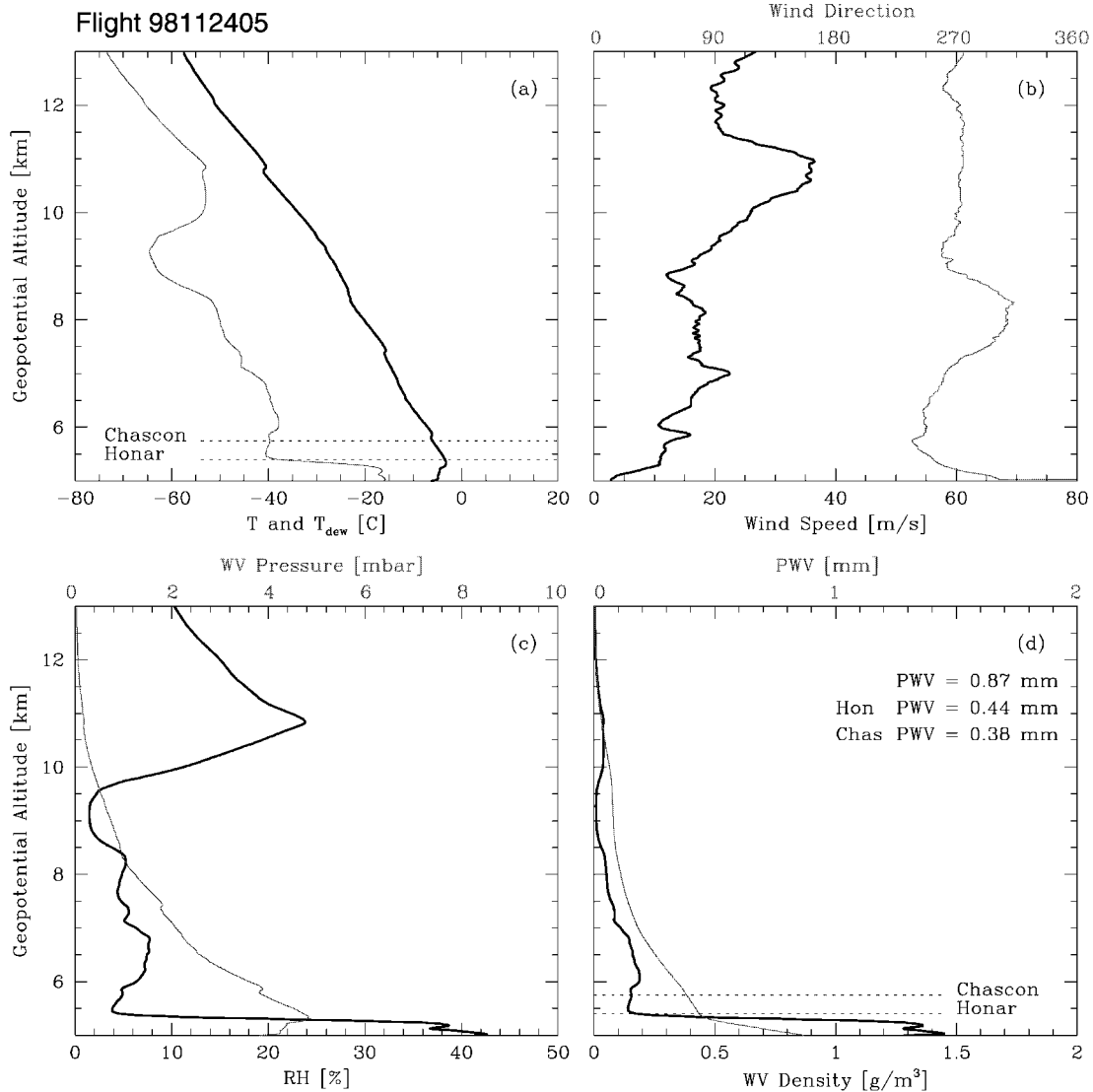


FIG. 6.—Radiosonde data for a 1998 November 24 launch, 0500 UT. Temperature inversion appears below 5.4 km. Panel description as in Fig. 4.

solar radiation, through the dissociation of ozone. Thus OH^- airglow originates at heights of 70–90 km and affects all ground-based locations, independently on altitude.

In addition to the atmospheric background, astronomical observations need to contend with cosmic backgrounds, such as that produced by the thermal emission and the scattering of solar photons by interplanetary dust, the interstellar dust emission, the cosmological microwave background radiation, and the thermal emission of the telescope and detectors themselves.

We next compute background levels for various atmospheric conditions; in doing so we follow the approach of Thronson et al. (1995).

Let's first consider the “near field” thermal background. In the atmospheric windows of interest the atmosphere is optically

thin, so that the specific intensity of the emitted radiation can be approximated by

$$I_\nu = \tau_\nu B_\nu = \frac{2\tau_\nu (h\nu^3/c^2)}{\exp(h\nu/kT) - 1}, \quad (2)$$

where B_ν is Planck's function and τ_ν the optical depth. Thus the number of photons per unit time, originating with the thermal background of temperature T and striking the telescope within the solid angle subtended by a point source Ω_{ps} , is

$$\mathcal{B} = I_\nu \mathcal{A} \Omega_{\text{ps}} \Delta\nu / h\nu, \quad (3)$$

where \mathcal{A} is the collecting area of the telescope and $\Delta\nu$ is the

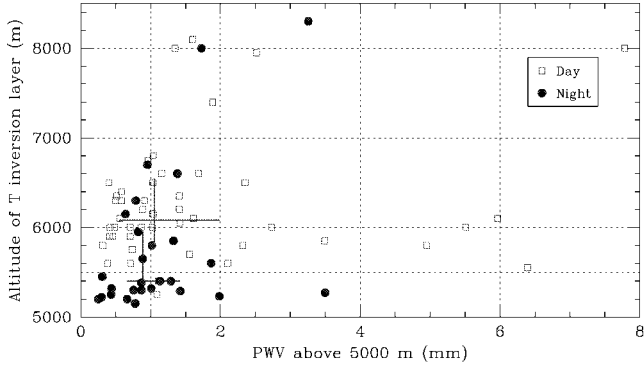


FIG. 7.—Altitude of temperature inversion layers identified in daytime (*open squares*) and nighttime (*filled circles*) radiosonde profiles. The large crosses are plotted at the median values of elevation and PWV; the span of the crosses' arm extends from first to third quartiles.

detection bandwidth. Converting to photoelectrons per second and assuming a detector gain of 1,

$$\mathcal{B}_e = 2.22 \times 10^{15} \frac{\mathcal{M} \times \text{QE}}{\mathcal{R} \lambda_\mu [\exp(1.44 \times 10^4 / \lambda_\mu T) - 1]} [e^{-1} \text{ s}^{-1}], \quad (4)$$

where T and QE are respectively the system transmission and quantum efficiency over the band, λ_μ the wavelength in μm , and $\mathcal{R} = \nu/\Delta\nu = \lambda/\Delta\lambda$. Equation (4) is derived assuming that the telescope is diffraction limited at all wavelengths, so that Ω_{ps} is the solid angle subtended by the ring corresponding to the first diffraction null and $\mathcal{A}\Omega_{\text{ps}}$ is then $3.7\lambda_\mu^2$. This assumption makes the background estimate independent on telescope aperture, allowing an intercomparison of different sites or atmospheric conditions. At the shorter wavelengths, at which the seeing angle is larger than the diffraction limit of the aperture, such an assumption is incorrect, and Ω_{ps} should be replaced with the solid angle which encircles 90% of the light within the seeing disk.

Different sources of thermal emission yield an additive contribution to \mathcal{B}_e . For the atmospheric thermal background, we approximate τ with the complement to one of the transparency as displayed in Figure 8. For the thermal emission of the telescope, we replace τ in equation (4) with a constant emissivity ϵ_{tel} .

As for the cosmic backgrounds, following Tokunaga (2000) and using equation (4), we approximate the zodiacal emission of dust by that of a blackbody with $T = 275$ K attenuated by $\epsilon = 7.1 \times 10^{-8}$, the sunlight scattered by the interplanetary particles by a blackbody of $T = 5800$ K and $\epsilon = 3 \times 10^{-14}$, the interstellar dust emission by a blackbody of $T = 17$ K and

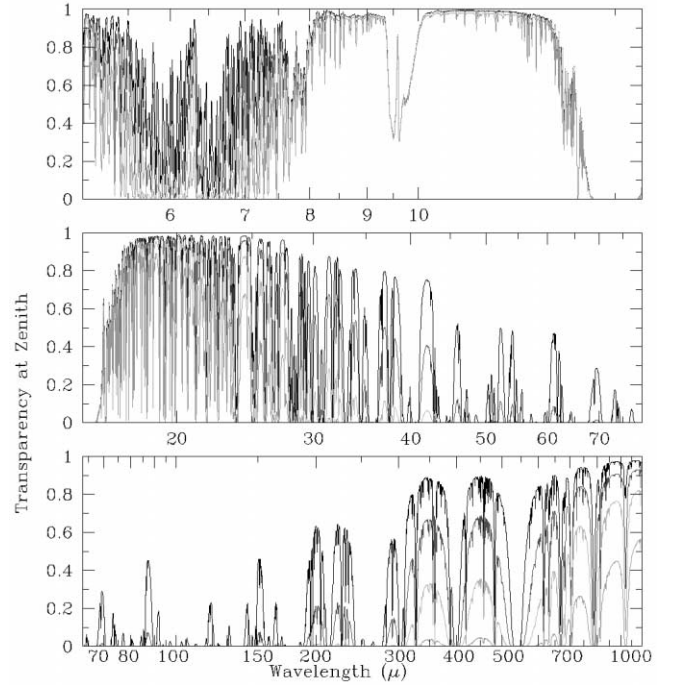


FIG. 8.—Atmospheric transparency at zenith between 5 and 1000 μm , for a site at an altitude of 5000 m and different H_2O column densities: the tracings, top to bottom, correspond to 0.1, 0.4, 1.0, and 3.0 mm of PWV.

$\epsilon = 10^{-3}$, and the cosmic microwave background by a blackbody with $T = 2.73$ K and $\epsilon = 1$.

Figure 9 illustrates the background \mathcal{B}_e for an Atacama telescope with $\epsilon_{\text{tel}} = 0.05$, estimated for the very best atmospheric conditions of $\text{PWV} = 0.2$ mm and a seeing of $0''.35$ at $0.5 \mu\text{m}$ (as shown in Table 1, $\text{PWV} = 0.2$ mm is the value for the lowest quartile at a high-elevation site, and seeing near $0''.35$ may have similar frequency at such a site; the chosen combination of values may occur in 5%–20% of the time, depending on how correlated seeing and PWV are; of eight reliable events of simultaneous radiosonde and seeing measurements, the four with $\text{PWV} < 1$ mm yield an average seeing of $0''.51$ at $0.5 \mu\text{m}$, while the other four, with $\text{PWV} > 1$ mm, have average seeing of $0''.84$; more data is needed to confirm this possible correlation). In the same figure, we also display estimates of the background for a space telescope passively cooled (e.g., the *Next Generation Space Telescope* [NGST]), a cryogenically cooled space telescope (e.g., the *Space Infrared Telescope Facility* [SIRTF]), and a stratospheric, telescope airborne at 12 km altitude (above which PWV is assumed to be $10 \mu\text{m}$, $\epsilon_{\text{tel}} = 0.15$, and image quality of $2''$ at $1 \mu\text{m}$ for the Stratospheric Observatory for Infrared Astronomy (SOFIA) (this may be an overestimate of image quality: while the optical quality of the instrument is high, pointing jitter and seeing produced by the turbulent airflow near the airplane may produce worse values). We have assumed a telescope temperature of 260 K for Atacama, 240

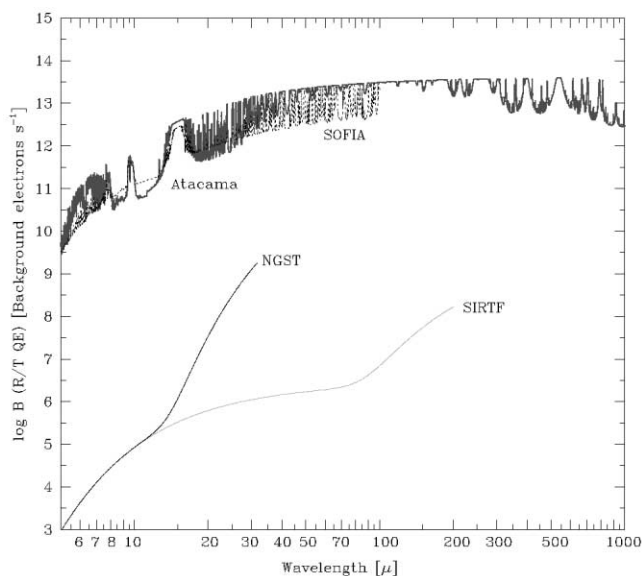


FIG. 9.—The total backgrounds for Atacama (very best atmospheric conditions with PWV = 0.2 mm and seeing of $0''.25$ assumed) and several space and airborne telescopes are compared. We have assumed that $\mathcal{M} \times \text{QE} \times G/R = 1$. See text for further details.

K for SOFIA, 60 K for *NGST*, and 5.5 K for *SIRTf*. The temperature of the emitting atmospheric layers was assumed to be 255 K for Atacama and 230 K for SOFIA. For simplicity, we assume $\mathcal{M} \times \text{QE} \times G/R = 1$, which overestimates the bandwidths that are possible in some of the atmospheric windows. Telescope and atmospheric thermal backgrounds dominate in the case of all ground-based instruments, while in the case of space instruments, even if not cryogenically cooled, the zodiacal emission dominates. Between 5 and 15 μm , for example, the *NGST* will have a background about 6 orders of magnitude lower than that for an Atacama telescope. While airborne at high altitude, the SOFIA telescope itself will produce substantial thermal emission and lower image quality than can be achieved from the ground. Note that the background in good Atacama conditions and for Sofia are comparable. SOFIA will, however, have access to atmospheric windows inaccessible from the ground.

5.2. Comparison of Broadband Sensitivities

The signal-to-noise ratio Q for a single integration of time t can in general be expressed as (Thronson et al. 1995)

$$Q = \frac{St}{[(S + \mathcal{B}_e + \mathcal{D})t + R^2 + N_c t^2]^{1/2}}, \quad (5)$$

where S is the source signal, \mathcal{D} is the detector dark current, R is its readout noise, and N_c is the signal produced by source confusion. A given signal, such as S , relates to the flux density

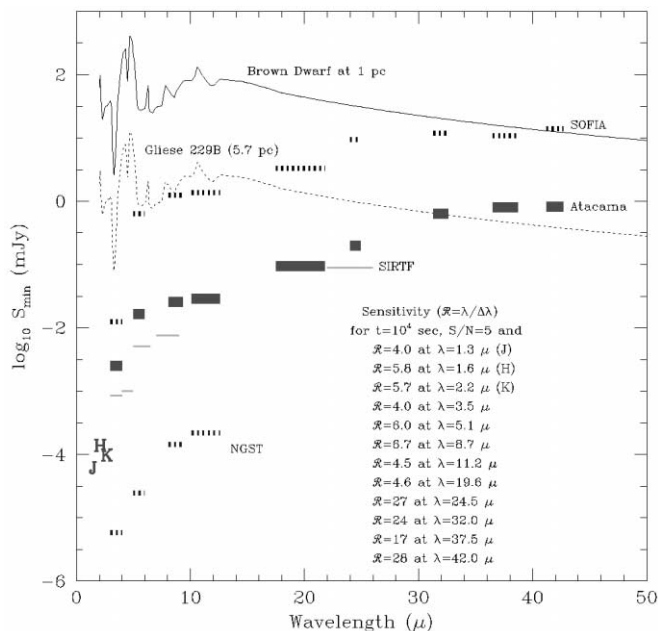


FIG. 10.—Comparison of sensitivities for several proposed or future telescopes, for a signal-to-noise ratio of 5 and an integration time of 10^4 s. The length of the horizontal bars identifying each wave band illustrates \mathcal{R} , as tabulated in the inset. See text for assumed telescope parameters. The Atacama telescope is assumed seeing limited with image size of $0''.25$. The labels *J*, *H*, and *K* refer to the Atacama sensitivities. The *J*-band limit is equivalent to about 26th magnitude. For reference, the spectral shape of a brown dwarf (Gliese 229B) has been plotted at the assumed distances of 1 and 5.7 pc. 1 mJy is $10^{-29} \text{ W m}^{-2} \text{ Hz}^{-1}$.

via

$$S(\text{mJy})e^{-\tau} = 6.63 \times 10^{-5} \frac{\mathcal{R}}{\text{QE} \times \mathcal{M} \times \mathcal{A}} S. \quad (6)$$

We adopt the following detector performance characteristics for the 3–40 μm range: $\text{QE} \approx 0.50$, $\mathcal{D} \approx 10 e^- \text{ s}^{-1}$, and $R \approx 50 e^- \text{ rms}$ (Thronson et al. 1995; G. Stacey 2000, private communication; B. Brandl & B. Pirger 2000, private communication); source confusion does not become an issue shortward of 50 μm , as we shall discuss in the next section. It is thus safe to assume that in the near- and mid-IR the thermal background dominates for broadband observations, so that the minimum detectable signal, for an exposure of time t achieving signal-to-noise Q , according to equation (5), is

$$S_{\text{min}} \approx Q[\mathcal{B}_e/t]^{1/2}. \quad (7)$$

We use equations (4) and (7) to estimate limiting fluxes for point sources, assuming $T = 0.4$ and, as indicated above, $\text{QE} = 0.5$. The broadest bandwidths usable are, of course, limited by atmospheric absorption. Sensitivities are computed for $Q = 5$ and exposures of $t = 10^4$ s. We underscore the fact

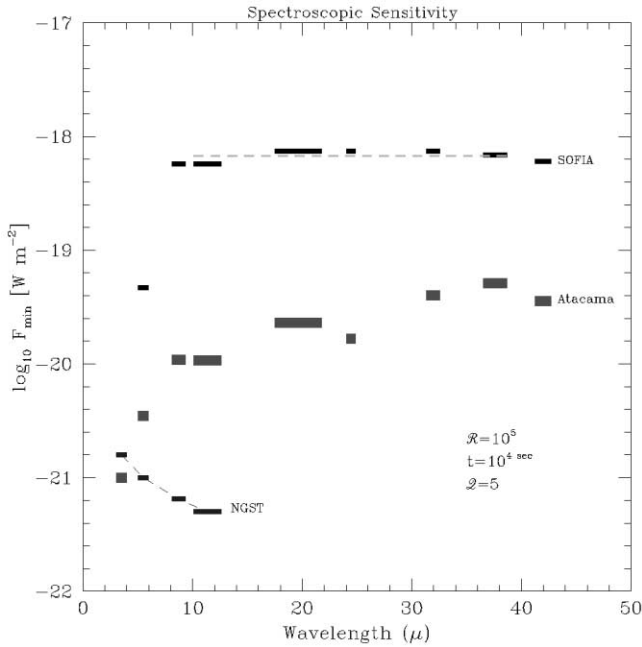


FIG. 11.—Spectral sensitivities for several proposed telescopes; for Atacama, calculations correspond to $\mathcal{R} = 10^5$, $Q = 5$, and $t = 10^4$ s. Note that for *SIRTF*, indicated by a horizontal dashed line, the resolution is only 600.

that the chosen bands are those accessible from the ground: *SOFIA*, *SIRTF*, and *NGST* will access spectral regions inaccessible from the ground. The results are plotted in Figure 10, for a telescope at Atacama with a diameter of 15 m, *NGST* with a diameter of 6 m, *SIRTF* with a diameter of 0.85 m, and *SOFIA* with a diameter of 2.4 m. In the case of the Atacama telescope, we have assumed that the image size is seeing-limited at $0''.35$ at $0.5 \mu\text{m}$. Note that with an adaptive optics system of moderate to good efficiency, the near-IR sensitivity can improve by 1 order of magnitude, beyond the limit in Figure 10, provided that it does not significantly increase the telescope emissivity. The implementation of an adaptive secondary would thus be desirable and that of a multiconjugate system would raise more serious emissivity concerns. The point-source sensitivity plotted in Figure 10 for *J* band is equivalent to 26th magnitude; with an adaptive optics system that limit would approach 29th magnitude. The telescope labels are the same as for Figure 9. The *SIRTF* sensitivities have been obtained from the *SIRTF* Web site⁵ and links referred therein. The *NGST* sensitivities have been plotted for the same bandpasses and \mathcal{R} as for the Atacama telescope, although it should be clear that the whole near-IR spectrum will be accessible to *NGST*. For comparison, we also plot the flux density curves of the brown dwarf Gliese 229B at source distances of 5.7 and 1 pc (Matthews et al. 1996).

The thermal background does not always constitute the main

limitation at submillimeter wavelengths. Source confusion can become important. The sky source density at far-IR and submillimeter wavelengths is relatively uncertain, but it is unlikely to be a concern even for large integrations ($\sim 10^4$ s) for large aperture telescopes (diameter greater than 10 m). Assuming $\mathcal{M} = 0.4$, $\text{QE} = 0.5$ (a quantum efficiency which can be approached by detectors with modern bolometers), and optimal atmospheric conditions as can be found in Atacama (PWV = 0.2 mm), an observation with $Q = 5$ and $t = 10^4$ s can reach a sensitivity on the order of 1 mJy at all the atmospheric windows between 300 μm and 1 mm, and about 3 mJy for those between 200 and 300 μm .

5.3. Comparison of Spectroscopic Sensitivities

Suppose the flux density contributed at a given frequency by a spectral line is S . The integrated flux over the whole line is $\int S d\lambda$. If the spectral line is unresolved, the flux associated with the line is $S\Delta\lambda = S\lambda/\mathcal{R}$, where S is now the mean line flux over the spectral channel which contains the line. If we measure the integrated flux in W m^{-2} , then the signal S in electrons per second can be converted to

$$F(\text{W m}^{-2}) = 2.0 \times 10^{-19} \frac{S}{\lambda_{\mu} \times A \times \text{QE} \times \mathcal{M}}. \quad (8)$$

In spectroscopic observations, the high \mathcal{R} reduces the impact of the high thermal background, as illustrated by equation (4). For observations with $\mathcal{R} = 10^5$, for example, the thermal background contribution, which is inversely proportional to \mathcal{R} , will be several orders of magnitude lower than in the case of photometric observations. Consider equation (5): \mathcal{B}_e can become comparable with or smaller than \mathcal{D} , in which case the observation will be limited by detector noise. For values of $\mathcal{D} \approx 10 e^- \text{ s}^{-1}$ and $R \approx 50 e^-$, the background can easily become negligible with respect to \mathcal{D} in space-based instruments. The readout noise on the other hand is likely not to play a role if exposures exceed a few hundred seconds, because then $R^2 < \mathcal{D}t$. We will assume here that R^2 and the source confusion term in the denominator of equation (5) are negligible.

The minimum detectable integrated line flux for an integration time t , with a signal-to-noise ratio Q , can be written, in analogy to equation (7), as

$$F_{\text{min}}(\text{W m}^{-2}) = 2.0 \times 10^{-19} \frac{Q}{\lambda \times \mu \mathcal{A} \times \text{QE} \times \mathcal{M}} \left(\frac{\mathcal{B}'}{t} \right)^{1/2}, \quad (9)$$

where \mathcal{B}' is $\mathcal{B}_e + \mathcal{D}$. Note that, for a space-based instrument, near 5 μm $\mathcal{B}_e \approx 5 \times 10^{-3} e^- \text{ s}^{-1}$ for $\mathcal{R} = 10^5$, so $\mathcal{B}_e \ll \mathcal{D}$, and the instrument is detector limited. In Figure 11, we show sensitivity limits computed using equation (9), for $\mathcal{R} = 10^5$, $\mathcal{D} = 10$, $\text{QE} = 0.5$, $T = 0.4$, and $Q = 5$, except for *SIRTF*, for which \mathcal{R} is only 600.

⁵ See the *SIRTF* home page (<http://sirtf.caltech.edu>).

6. CONCLUSIONS

The water vapor distribution above the Chajnantor plateau appears to have the following properties:

1. The median PWV above the plateau at 5000 m is ~ 1.2 mm. Variations from year to year can be as large as 50% of that value.
2. Seasonal variations in PWV are also large: median values for the 8 months from April to November are 30% lower than the yearly median, while median values for the summer months may be more than twice as large.
3. PWV varies by about $\pm 20\%$ with the daily cycle, with a phase lag about 4 hours behind that of sunlight: minimum PWV occurs between midnight and noon, and maximum occurs at sunset.
4. The distribution of the water vapor of the median atmosphere over Chajnantor is well approximated by an exponential, with a scale height of 1.13 km. At any given time, however, the water vapor distribution can depart from an exponential shape, more dramatically when temperature inversions occur.

The thickness of the water vapor layer appears to vary in phase with the solar illumination cycle by about $\pm 25\%$; minimum is near local midnight.

The implications of these effects for summits in the vicinity of the Chajnantor Plateau are as follows:

1. The median PWV above 5400 m elevation drops by one-third with respect to the value measured at the plateau; above an elevation of 5750 m it drops by a factor of 2.
2. Median PWV in winter nights at a summit near 5400 m, such as Cerro Honar, may be as low as 0.5–0.6 mm, if conditions near the summit approach those of the free atmosphere. The lowest quartile of PWV may approximate 0.35–0.40 mm.
3. Median PWV in winter nights at a summit near 5700 m, such as Cerro Chascón, may approximate 0.40 mm, and the lowest quartile is near 0.20–0.25 mm.

Low-elevation temperature inversions are more likely during nighttime. During those episodes, much of the PWV is trapped below the inversion layer, and mountain peaks are offered a

nearly dry atmosphere, possibly endowed with high-quality seeing.

The conclusions listed above rely on still relatively sparse data from 108 radiosondes and should be considered as preliminary. However, these results suggest that exceptional possibilities for ground-based IR and submillimeter astronomical observations exist in the Llano de Chajnantor region. The combination of low water vapor content and high-quality seeing allow for low atmospheric background in the near- and mid-IR. At a telescope on a summit in the vicinity of the Chajnantor plateau, numerous atmospheric windows would appear in the mid-IR, up to about $50 \mu\text{m}$. In the far-IR and submillimeter regime, the 350, 450, 600, 750, and $870 \mu\text{m}$ windows reach exceptional transparency, while two useful windows appear near $200 \mu\text{m}$. Broadband observations with a 15 m class telescope at such a site would be close in sensitivity to those made with *SIRTF* in the mid-IR, offering a superb synergy match for follow-up observations of the *SIRTF* surveys. The near- and mid-IR performance of such a ground-based telescope in high-resolution spectroscopic mode would be exceptional and could be exceeded only by that of a space telescope of comparable aperture. The relative ease and cost-effectiveness of operation in the Atacama advises that serious attention be given to the Atacama sites for the installation of the next generation of large infrared telescopes.

The support and assistance of Joe Veverka, Yervant Terzian, Bob Richardson, Jennifer Yu, and Bryan Isacks of Cornell University; Martha Haynes of Cornell University and Associated Universities, Inc.; Robert L. Brown, Eduardo Hardy, and Geraldo Valladares of NRAO; the use of radiosonde data obtained through a collaboration with NRAO (Simon Radford and Bryan Butler), ESO (Angel Otarola), and SAO (Ray Blundell and Scott Paine); access to 225 MHz radiometry data of NRAO (Simon Radford); Don Tomás Poblete Alay and the staff of La Casa de Don Tomás are thankfully acknowledged. This study was made possible by a grant of the Provost's Office of Cornell University and the National Science Foundation grant AST 99-10136.

REFERENCES

- Delgado, G., Otarola, A., Belitsky, V. & Urbain, D. 1999, preprint
 Giovanelli, R., et al. 2001, *PASP*, 113, 789 (Paper I)
 Holdaway, M. A., Ishiguro, M., Foster, S., Kawabe, K., Kohno, K.,
 Radford, S. & Saito, M. 1996a, MMA Memo 152 (Tucson: NRAO)
 Holdaway, M. A., Ishiguro, M., Nakai, N. & Matsushita, S. 1996b,
 MMA Memo 158 (Tucson: NRAO)
 Hufnagel, R. E. 1978, in *The Infrared Handbook*, ed. W. L. Wolfe &
 G. J. Zissis (Washington, DC: US GPO), chap. 6
 Matthews, K., Nakajima, T., Kulkarni, S. R. & Oppenheimer, B. R.
 1996, *AJ*, 112, 1678
 McPhaden, M. J. 1999, *Science*, 283, 950
 Thronson, H. A., Jr., Rapp, D., Bailey, B., & Hawarden, T. G. 1995,
PASP, 107, 1099
 Tokunaga, A. T. 2000, in *Astrophysical Quantities*, ed. A. Cox (4th
 ed.; Berlin: Springer), 143
 Wolfe, W. L. & Zissis, G. J. 1978, *The Infrared Handbook* (Wash-
 ington, DC: Dept. Navy, Office Naval Res.)